



Robust path control for an autonomous ground vehicle in rough terrain

Jongho Shin^{a,*}, Dongjun Kwak^b, Taehyung Lee^b

^a Mechanical Engineering, Chungbuk National University, Cheongju, Republic of Korea

^b Agency for Defense Development, Daejeon, Republic of Korea

ARTICLE INFO

Keywords:

Autonomous ground vehicle
Robust control
Disturbance observer
Optimal tire force distribution

ABSTRACT

Typically, it is not trivial for an autonomous ground vehicle (AGV) to navigate in rough terrain due to lots of unexpectable uncertainties. Because the performance of the autonomous navigation can be degraded by the uncertainties, the AGV requires a robust control system against them. To handle the necessity, this study proposes the robust path controller by utilizing a disturbance observer (DOB)-based control method. The proposed controller is developed by two steps: the first step is to design a controller for handling a nominal system of the AGV, and the other is to add the DOB to the nominal controller. Then, the determined control input is distributed into tire forces because the tire forces are final resource enabling the AGV to move. The tire force distribution is defined as an optimization problem with some constraints, and the solution is obtained by the CVXGEN. Finally, numerical simulations and field tests with a skid-type ground vehicle, developed by the authors' laboratory, are conducted to validate the performance of the proposed method.

1. Introduction

For last several decades, an autonomous ground vehicle (AGV) has obtained a great deal of attention from lots of automobile research groups because it is viewed as a plausible method to enhance safety of human, improve performance of a military mission/planetary exploration (Iagnemma & Dubowsky, 2004) or decrease fuel consumption (Gonzalez, Perez, Milanes, & Nashashibi, 2016; Katrakazas, Qudus, Chen, & Deka, 2015). With these attentions, a flurry of results have been developed using various ideas (Gonzalez et al., 2016; Katrakazas et al., 2015; Thrun et al., 2006). In general, the autonomous navigation system is composed of three main components such as planning (Shin, Kwak, & Kwak, 2020), perception (Sock, Kim, Min, & Kwak, 2016) and control. Among those components, this study focuses on the control component for the AGV in rough terrain.

The control methods in the references can be divided into two groups. In the first group, the path controller is developed to track given position trajectory command dependent on time (Huang, Wen, Wang and Jiang, 2014; Kayacan, Ramon, & Saeys, 2016). Because the given trajectory reference is composed of three elements, i.e., x , y position components and heading angle commands of the AGV, while the control inputs for the AGV are generally composed of longitudinal force and lateral moment, the path control problem is a typical under-actuated control problem. To handle this problem effectively, various ideas have been developed and their performance has been validated with lots of numerical simulations. Even though there exist several experiment results (Kayacan et al., 2016; Yi, Song, Zhang, & Goodwin,

2007), it is not trivial to validate the performance of those kinds of the control methods with the experiments because, in practice, it is difficult or meaningless to give the time-dependent position trajectory command to the AGV appropriately at all situation.

The other approach is to design the path controller for following the given velocity and heading angle commands (Huang, Zhang, Zhang and Wang, 2014; Kang, Kim, Lee, & Yi, 2010). This approach has been studied a lot in the practical research fields because the velocity and heading angle commands can be generated simply or intuitively, comparing to the time-dependent commands. Especially, because the dynamic model of a steering-type ground vehicle can be divided into longitudinal (velocity) and lateral (yaw motion) subsystems, the velocity and heading angle controllers for the steering-type vehicle can be developed separately. While the velocity control for the steering-type ground vehicle is relatively simple, the lateral controller has been developed with various ideas because it is not trivial to control the lateral motion satisfactorily. In Urmson et al. (2006), a heading reference command was followed by a proportional-integral-derivative (PID) controller. A robust control method with continuous control input was designed for the lateral motion of the AGV and validated in Shin, Huh, and Park (2015), and a robust gain scheduling method was proposed to control the time-varying nonlinear lateral vehicle model in Zhang, Zhang, and Wang (2014). In Huang, Zhang et al. (2014), the lateral motion controller was developed to consider a steering system with the backlash-type hysteresis.

On the other hand, this study handles a skid-type ground vehicle with six tires, developed by the authors' laboratory as shown in Fig. 1.

* Corresponding author.

E-mail address: jshin@cbnu.ac.kr (J. Shin).



Fig. 1. Autonomous ground vehicle.

Due to the skid-type property, its lateral motion is available only using torque or wheel velocity difference between left and right tires. This means that the longitudinal and lateral dynamic motions of the skid-type ground vehicle are strongly coupled, i.e., the final control forces for the longitudinal and lateral motions are generated by all the tires of the AGV. Thus, unlike the steering-type ground vehicle, it is not possible to develop the path controller separately, and the path controller for considering both the longitudinal and lateral motions simultaneously is required. In addition, the path controller should be as robust as possible under the uncertain environment because the authors' AGV is operated in the rough terrain.

To handle the longitudinal and lateral motions simultaneously, this study proposes the robust controller by utilizing a disturbance observer (DOB)-based control method (Chen, Komoda, & Fukuda, 2000; Kim, Seo, Shin, & Kim, 2018). It is well known that the DOB-based controller assures satisfactory transient and steady state performance, and recovers nominal performance of the uncertain nonlinear system (Back & Shim, 2008, 2009). By employing the advantages of the DOB-based control method, the path control system, i.e., velocity and heading angle control system is proposed in this study. The proposed controller

is developed by two steps: the first step is to design a controller for handling a nominal model of the AGV, and the other is to add the DOB to the nominal controller. By adding the DOB to the nominal controller, the nominal performance of the uncertain AGV system is recovered, and the velocity and heading angle errors are bounded less than or equal to a given ϵ . On the other hand, the final control input for enabling the AGV to move is tire force. Thus, the control input obtained by the DOB-based controller should be distributed into six tire forces. To handle this problem, this study defines an optimal tire force distribution problem and its solution is obtained by employing the CVXGEN tool (Mattingale & Boyd, 2018). Finally, to validate the performance of the proposed method, numerical simulations with TruckSim software (TruckSim, 0000a) and field tests are performed, and the results are analyzed.

To sum up, the main contribution of this study is summarized as

- The integrated path control law for the skid-type ground vehicle is proposed using the DOB-based nonlinear control method.
- The stability of the proposed controller is thoroughly analyzed using the Lyapunov stability theory.
- The proposed method was validated using the numerical simulations and field tests in the rough terrain.

On the other hand, the proposed control method is utilized in the autonomous navigation of the AGV in the rough terrain. Fig. 2 presents the overall diagram of the autonomous navigation system developed by the authors' laboratory. The architecture is composed of three main components: perception, planning and control components. In addition, an operating control system (by an operator) is developed to transmit objective points, velocity command and start/stop command for the autonomous navigation to the AGV, and receive the information of the vehicle. For the autonomous navigation, the operator chooses several mid/goal points and determines the velocity command of the AGV. This information is transmitted to the AGV by wireless communication. Based on this information, the global path planning (GPP) is first performed and then, the local path planning (LPP) (Shin et al., 2020) is conducted with the GPP and environment perception results (Sokk et al., 2016). After the traversability analysis is done with the LPP and perception results (Hong et al., 2016, 2017), the velocity and heading angle commands are finally determined and those references are transmitted to the path control component developed in this study. The detailed explanation is described in Shin et al. (2020).

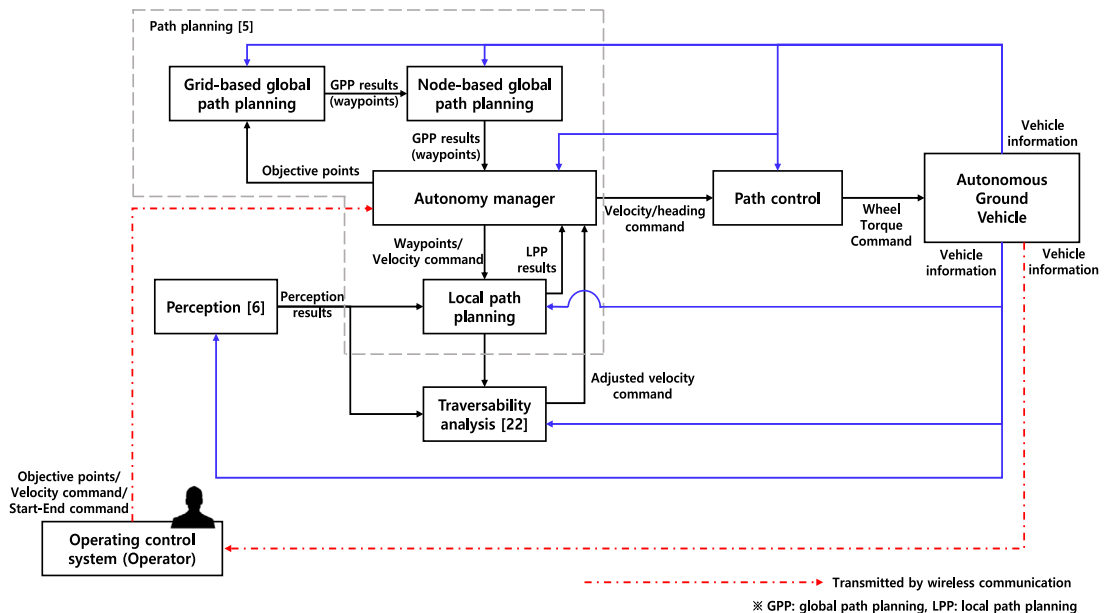


Fig. 2. Schematic diagram of autonomous navigation system in rough terrain: Vehicle information is composed of the position, velocity, acceleration, attitude and angular rate, etc.

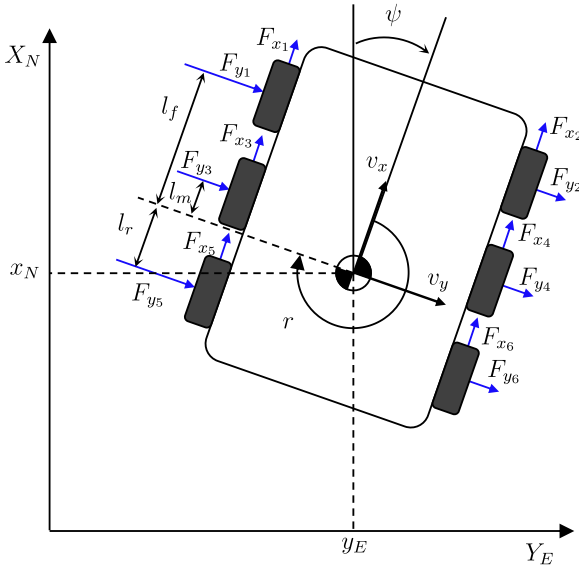


Fig. 3. Base structure and coordinate frames.

This paper is organized as follows: a dynamic model of the skid-type AGV is described in Section 2. Then, Section 3 proposes the DOB-based controller and its closed loop stability is analyzed using the Lyapunov stability theory. In addition, the optimization problem for the tire force distribution is proposed and its solution is obtained. To validate the performance of the proposed method, numerical simulations and field tests are conducted, and their results are analyzed in Section 4. Finally, conclusions are presented in Section 5.

2. Vehicle model

In general, it is not trivial to develop the path controller for the AGV using a full nonlinear dynamic vehicle model because there exist lots of unknown nonlinear terms such as interactive forces between the vehicle and ground, and coupling effects between longitudinal and lateral motions. A simplified dynamic model, instead of the nonlinear model, is generally used for the controller design, and the differences between the real nonlinear system and simplified dynamic model are removed or compensated by the controller. This study employs a reduced dynamic model of the skid-type AGV for the controller design as well.

The employed skid-type AGV in Fig. 3, developed by the authors' research laboratory, has six in-wheel-motors (6 wheel drive). The simplified dynamic model of the AGV is represented as

$$\begin{aligned} m(\dot{v}_x - rv_y) &= F_x + \Delta_x, \\ m(\dot{v}_y + rv_x) &= F_y + \Delta_y, \\ \dot{\psi} &= r, \\ I_z \dot{r} &= M_z + \Delta_z \end{aligned} \quad (1)$$

where

$$\begin{aligned} F_x &= \sum_{i=1}^6 F_{x_i}, \\ F_y &= \sum_{i=1}^6 F_{y_i}, \\ F_{y_{1,2}} &= -c_f \tan^{-1} \left(\frac{v_y + l_f r}{v_x} \right) \\ F_{y_{3,4}} &= -c_m \tan^{-1} \left(\frac{v_y + l_m r}{v_x} \right) \\ F_{y_{5,6}} &= -c_r \tan^{-1} \left(\frac{v_y - l_r r}{v_x} \right) \end{aligned}$$

and

$$\begin{aligned} M_z &= \frac{t_w}{2} (F_{x_1} - F_{x_2} + F_{x_3} - F_{x_4} + F_{x_5} - F_{x_6}) \\ \Delta_z &= M_y + \Delta_r, \\ M_y &= l_f(F_{y_1} + F_{y_2}) + l_m(F_{y_3} + F_{y_4}) - l_r(F_{y_5} + F_{y_6}) \end{aligned}$$

The variable v_x, v_y are longitudinal and lateral velocities in the body frame, ψ, r are heading angle and yaw rate of the AGV, and F_x, F_y, M_z denote longitudinal/lateral forces and lateral moment, respectively. The parameters m, I_z, c_i are mass, moment of inertia and cornering stiffness of a tire, respectively. Those values are unknown but, their nominal values are known. The terms $\Delta_x, \Delta_y, \Delta_z$ denote unknown uncertainties. The total force F_x and lateral moment M_z are defined using 6 wheel forces F_{x_i} . Thus, the control inputs for the model (1) are defined as the longitudinal force F_x and lateral moment M_z .

As addressed in Section 1, the objective of the path control in this study is to follow the given velocity and heading angle commands. Thus, several formal assumptions are exploited to develop subsequent controller design and analysis.

Assumption 1. Let v_d and ψ_d be the reference commands for the velocity and heading angle, respectively, and $v_d, \dot{v}_d, \psi_d, \dot{\psi}_d$ and $\ddot{\psi}_d$ be continuous and bounded.

Assumption 2. The unknown terms m, I_z and unknown uncertainties $\Delta_x, \Delta_y, \Delta_z$ are bounded and have bounded derivatives (but the bounds can be arbitrarily large).

Assumption 3. The dynamic system

$$m(\dot{v}_y + rv_x) = F_y + \Delta_y$$

is input-to-state stable (ISS) with respect to constrained inputs v_x and r .

It is naturally acceptable to assume the boundedness of the uncertainties ($\Delta_x, \Delta_y, \Delta_z$) and their derivative because it is not possible to obtain or assure the physically reasonable dynamic motion of the AGV without Assumption 2. In addition, because the lateral force F_y is dependent on the longitudinal velocity v_x and yaw rate r , the lateral velocity v_y is bounded if the states v_x and r , i.e., inputs, for the dynamic motion v_y are bounded.

3. Development of robust path control system

The robust path controller is developed by two steps: the first step is to design a controller for a nominal model and the second step is to add the disturbance observer to the developed nominal controller. Then, the determined control inputs F_x, M_z are optimally distributed to six wheel traction forces. The overall control structure is presented in Fig. 4.

3.1. Nominal controller design

The first step is to design the velocity and heading angle controllers using the nominal model about the dynamics (1) as follows:

$$\dot{v}_x = \frac{1}{\bar{m}} F_{x_n}, \quad \dot{r} = \frac{1}{\bar{I}_z} M_{z_n}$$

where \bar{m}, \bar{I}_z denote the nominal values of m and I_z , respectively. To satisfy the control objectives, define two error values as follows:

$$e_v = v_d - v_x, \quad e_{\psi_1} = \psi_d - \psi \quad (2)$$

where v_d, ψ_d denote the velocity and heading angle commands, respectively. By differentiating the error variables e_v, e_{ψ_1} with respect to time, we obtain

$$\dot{e}_v = \dot{v}_d - \dot{v}_x$$

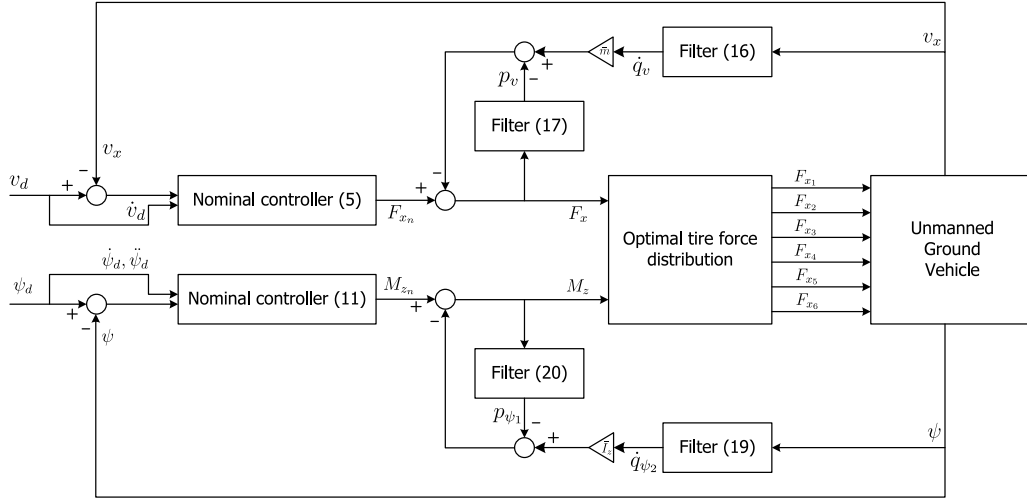


Fig. 4. Schematic diagram of the proposed path control system.

$$= \dot{v}_d - \frac{1}{\bar{m}} F_{x_n}$$

and

$$\begin{aligned} \dot{e}_{\psi_1} &= \dot{\psi}_d - \dot{\psi} \\ &= \dot{\psi}_d - r. \end{aligned}$$

Based on the Eq. (3), the nominal velocity controller is designed as

$$F_{x_n} = \bar{m}(k_v e_v + \alpha_v \dot{v}_d) \quad (5)$$

where $k_v > 0, \alpha_v \geq 1$ to be determined later. By injecting the control law (5) to the Eq. (3), the closed loop error system for the velocity is represented as

$$\dot{e}_v = (1 - \alpha_v) \dot{v}_d - k_v e_v. \quad (6)$$

Unlike the variable \dot{e}_v , the error \dot{e}_{ψ_1} does not include the control input. Thus, a virtual control input is introduced to develop the heading angle controller as follows

$$\begin{aligned} \dot{e}_{\psi_1} &= \dot{\psi}_d - r \\ &= \dot{\psi}_d - \bar{r} + \bar{r} - r \\ &= \dot{\psi}_d + e_{\psi_2} - \bar{r} \end{aligned} \quad (7)$$

where \bar{r} is the virtual control input and $e_{\psi_2} = \bar{r} - r$. If the virtual control input \bar{r} is designed as

$$\bar{r} = \dot{\psi}_d + k_{\psi_1} e_{\psi_1} \quad (8)$$

and injected to the Eq. (7), the variable \dot{e}_{ψ_1} is represented as

$$\dot{e}_{\psi_1} = -k_{\psi_1} e_{\psi_1} + e_{\psi_2} \quad (9)$$

where $k_{\psi_1} > 0$. Then, the error e_{ψ_2} is differentiated with respect to time as follows

$$\begin{aligned} \dot{e}_{\psi_2} &= \dot{\bar{r}} - \dot{r} \\ &= \ddot{\psi}_d + k_{\psi_1} \dot{e}_{\psi_1} - \frac{1}{I_z} M_{z_n}. \end{aligned} \quad (10)$$

With the above equation, the nominal heading angle controller is designed as

$$M_{z_n} = \bar{I}_z (k_{\psi_1} \dot{e}_{\psi_1} + k_{\psi_2} e_{\psi_2} + \alpha_\psi \ddot{\psi}_d) \quad (11)$$

where $k_{\psi_2} > 0, \alpha_\psi \geq 1$ to be determined later. Based on the control input (11), the closed loop heading angle error system is represented as

$$\dot{e}_{\psi_2} = (1 - \alpha_\psi) \ddot{\psi}_d - k_{\psi_2} e_{\psi_2}. \quad (12)$$

Thus, the closed loop error dynamics related to the nominal model are represented as

$$\dot{e}_v = -k_v e_v + (1 - \alpha_v) \dot{v}_d,$$

$$\dot{e}_\psi = A_\psi e_\psi + B_\psi (1 - \alpha_\psi) \ddot{\psi}_d \quad (13)$$

where $e_\psi = [e_{\psi_1} \ e_{\psi_2}]^T$ and

$$A_\psi = \begin{bmatrix} -k_{\psi_1} & 1 \\ 0 & -k_{\psi_2} \end{bmatrix}, B_\psi = \begin{bmatrix} 0 \\ 1 \end{bmatrix}.$$

If the Lyapunov candidate function V_n is determined as

$$V_n = \frac{1}{2} e_v^2 + \frac{1}{2} e_\psi^T P_\psi e_\psi \quad (14)$$

where $A_\psi^T P_\psi + P_\psi A_\psi = -2k_\psi I_2$ and $k_\psi \geq 1$ to be determined later, its directional time derivative along the error dynamics (13) is represented as

$$\begin{aligned} \dot{V}_n &= -k_v e_v^2 + e_v (1 - \alpha_v) \dot{v}_d - k_\psi e_\psi^T e_\psi + e_\psi^T P_\psi B_\psi (1 - \alpha_\psi) \ddot{\psi}_d \\ &\leq -k_v e_v^2 + d_v |e_v| - k_\psi \|e_\psi\|^2 + d_\psi \|e_\psi\| \end{aligned} \quad (15)$$

where $d_v := \max_t |(1 - \alpha_v) \dot{v}_d(t)|$ and $d_\psi := \max_t \|P_\psi\| |(1 - \alpha_\psi) \ddot{\psi}_d(t)|$.

Remark 1. In (15), the time derivative \dot{V}_n is represented as

$$\dot{V}_n \leq -\lambda_n \|Y_n\|^2 + \kappa_n \|Y_n\|$$

where $Y_n \triangleq [e_v \ e_\psi]^T$, $\lambda_n \triangleq \min\{k_v, k_\psi\}$, $\kappa_n \triangleq d_v + d_\psi$. Thus, if $\|Y_n\| \geq \kappa_n / \lambda_n$, $\dot{V}_n < 0$. With this property, we obtain that, for a given ϵ , it is always possible to choose k_v, k_ψ for assuring errors e_v, e_ψ less than or equal to ϵ .

3.2. Addition of disturbance observer to nominal controller

The nominal controller (5), (11) is designed using the uncertainty-free model of the AGV. To compensate the model difference between the nominal model and actual system, we add an internal controller to the developed nominal controller as shown in Fig. 4. The inner-loop controller with the DOB is developed as

• Velocity controller

$$\dot{q}_v = -\frac{a_v}{\tau_v} q_v + \frac{a_v}{\tau_v} v_x, \quad (16)$$

$$\dot{p}_v = -\frac{a_v}{\tau_v} p_v + \frac{a_v}{\tau_v} F_x, \quad (17)$$

$$F_x = p_v - \bar{m} \dot{q}_v + F_{x_n}, \quad (18)$$

• Heading angle controller

$$\begin{aligned}\dot{q}_{\psi_1} &= q_{\psi_2}, \\ \dot{q}_{\psi_2} &= -\frac{a_{\psi_0}}{\tau_\psi^2} q_{\psi_1} - \frac{a_{\psi_1}}{\tau_\psi} q_{\psi_2} + \frac{a_{\psi_0}}{\tau_\psi^2} \psi, \end{aligned} \quad (19)$$

$$\begin{aligned}\dot{p}_{\psi_1} &= p_{\psi_2}, \\ \dot{p}_{\psi_2} &= -\frac{a_{\psi_0}}{\tau_\psi^2} p_{\psi_1} - \frac{a_{\psi_1}}{\tau_\psi} p_{\psi_2} + \frac{a_{\psi_0}}{\tau_\psi^2} M_z, \end{aligned} \quad (20)$$

$$M_z = p_{\psi_1} - \bar{I}_z \dot{q}_{\psi_2} + M_{z_n} \quad (21)$$

where positive constants $a_i (i = v, \psi_0, \psi_1), \tau_j (j = v, \psi)$ are the design parameters to be determined for satisfying some stability criterion.

To analyze the inner loop structure in depth, state variables $p_i, q_i (i = v, \psi)$ are transformed into ξ_i and η_i as follows:

$$\xi_v = [q_v - v_x], \quad \eta_v = [p_v - \bar{m} \dot{q}_v], \quad (22)$$

$$\xi_\psi = \begin{bmatrix} \xi_{\psi_1} \\ \xi_{\psi_2} \end{bmatrix} = \begin{bmatrix} \frac{1}{\tau_\psi} q_{\psi_1} + \frac{a_{\psi_1}}{a_{\psi_0}} q_{\psi_2} - \frac{1}{\tau_\psi} \psi \\ q_{\psi_2} - r \end{bmatrix}, \quad (23)$$

$$\eta_\psi = \begin{bmatrix} \eta_{\psi_1} \\ \eta_{\psi_2} \end{bmatrix} = \begin{bmatrix} p_{\psi_1} - \bar{I}_z \dot{q}_{\psi_2} \\ \tau_\psi (p_{\psi_2} - \bar{I}_z \dot{q}_{\psi_2}) \end{bmatrix}. \quad (24)$$

Then, the dynamics of the transformed coordinates are represented as a standard singular perturbation form such as

$$\tau_v \dot{\xi}_v = -a_v \xi_v - \tau_v \dot{v}_x \quad (25)$$

$$\tau_v \dot{\eta}_v = -a_v \eta_v + a_v (F_x - \bar{m} \dot{v}_x) \quad (26)$$

$$\tau_\psi \dot{\xi}_\psi = A_{\xi_\psi} \xi_\psi - \tau_\psi B_{\psi_2} \dot{r} \quad (27)$$

$$\tau_\psi \dot{\eta}_\psi = A_{\eta_\psi} \eta_\psi + B_{\psi_2} a_{\psi_0} (M_z - \bar{I}_z \dot{r}) \quad (28)$$

where

$$A_{\xi_\psi} = \begin{bmatrix} -a_{\psi_1} & 1 \\ -a_{\psi_0} & 0 \end{bmatrix}, \quad A_{\eta_\psi} = \begin{bmatrix} 0 & 1 \\ -a_{\psi_0} & -a_{\psi_1} \end{bmatrix},$$

$$B_{\psi_2} = [0 \ 1]^T.$$

The quasi-steady states of ξ_i and η_i can be derived by putting $\tau_i = 0$ in Eqs. (25)–(28). They are denoted as ξ_i^* and η_i^* , respectively, and computed as $\xi_v^* = 0, \xi_\psi^* = 0_{21}, \eta_v^* = 0$ and

$$\eta_{\psi_1}^* = m \bar{m}^{-1} F_{x_n} - F_{x_n} - m r v_y - \Delta_x \quad (29)$$

$$\eta_{\psi_1}^* = \bar{I}_z^{-1} I_z M_{z_n} - M_{z_n} - \Delta_z. \quad (30)$$

With the equilibriums $\eta_v^*, \eta_{\psi_1}^*$, the control inputs F_x, M_z in Eqs. (18), (21) are rearranged as

$$\begin{aligned}F_x &= \eta_v + F_{x_n} \\ &= \eta_v - \eta_v^* + \eta_v^* + F_{x_n} \\ &= \tilde{\eta}_v + m \bar{m}^{-1} F_{x_n} - F_{x_n} - m r v_y - \Delta_x + F_{x_n} \\ &= \tilde{\eta}_v + m \bar{m}^{-1} F_{x_n} - m r v_y - \Delta_x \end{aligned} \quad (31)$$

$$\begin{aligned}M_z &= \eta_{\psi_1} + M_{z_n} \\ &= \eta_{\psi_1} - \eta_{\psi_1}^* + \eta_{\psi_1}^* + M_{z_n} \\ &= \tilde{\eta}_{\psi_1} + \bar{I}_z^{-1} I_z M_{z_n} - M_{z_n} - \Delta_z + M_{z_n} \\ &= \tilde{\eta}_{\psi_1} + \bar{I}_z^{-1} I_z M_{z_n} - \Delta_z \end{aligned} \quad (32)$$

where $\tilde{\eta}_v \triangleq \eta_v - \eta_v^*$ and $\tilde{\eta}_{\psi_1} \triangleq \eta_{\psi_1} - \eta_{\psi_1}^*$. When the control inputs (31) and (32) are injected to the real dynamics (1), we obtain the following systems

$$\begin{aligned}\dot{v}_x &= \frac{1}{m} \left(\tilde{\eta}_v + \bar{m}^{-1} m F_{x_n} - m r v_y - \Delta_x \right) + r v_y + \frac{1}{m} \Delta_x \\ &= \frac{1}{m} \tilde{\eta}_v + \frac{1}{m} F_{x_n}, \\ \dot{r} &= \frac{1}{I_z} \left(\tilde{\eta}_{\psi_1} + \bar{I}_z^{-1} I_z M_{z_n} - \Delta_z \right) + \frac{1}{I_z} \Delta_z \end{aligned} \quad (33)$$

$$= \frac{1}{I_z} \tilde{\eta}_{\psi_1} + \frac{1}{I_z} M_{z_n}. \quad (34)$$

Based on $\eta_v^*, \eta_{\psi_1}^*$ and the rearranged dynamics (33) and (34), the boundary layer model of the inner loop structure is represented in the singular perturbation form as follows:

$$\tau_v \dot{\xi}_v = -a_v \xi_v - \tau_v \left(m^{-1} \tilde{\eta}_v + \bar{m}^{-1} F_{x_n} \right) \quad (35)$$

$$\tau_v \dot{\eta}_v = -a_v m^{-1} \bar{m} \tilde{\eta}_v - \tau_v \dot{\eta}_v^* \quad (36)$$

$$\tau_\psi \dot{\xi}_\psi = A_{\xi_\psi} \xi_\psi - \tau_\psi B_{\psi_2} \left(\bar{I}_z^{-1} \tilde{\eta}_{\psi_1} + \bar{I}_z^{-1} M_{z_n} \right) \quad (37)$$

$$\tau_\psi \dot{\eta}_\psi = A_{\eta_\psi} \tilde{\eta}_\psi - B_{\psi_2} a_{\psi_0} \bar{I}_z^{-1} \tilde{\eta}_{\psi_1} - \tau_\psi B_{\psi_1} \dot{\eta}_{\psi_1}^* \quad (38)$$

where

$$A_{\tilde{\eta}_\psi} = \begin{bmatrix} 0 & 1 \\ 0 & -a_{\psi_1} \end{bmatrix}, \quad B_{\psi_1} = [1 \ 0]^T.$$

To prove the stability of the boundary layer models, we first check the elements $-a_v, -a_v m^{-1} \bar{m}, A_{\xi_\psi}, A_{\tilde{\eta}_\psi}$. Because $a_v > 0, m^{-1} \bar{m} > 0$ and A_{ξ_ψ} is Hurwitz, we can find the positive constants $\gamma_{\xi_v}, \gamma_{\tilde{\eta}_v}$ and positive definite matrix $P_{\xi_\psi} (\in \mathbb{R}^{2 \times 2})$ that satisfy

$$-\gamma_{\xi_v} a_v = -1, \quad -\gamma_{\tilde{\eta}_v} a_v m^{-1} \bar{m} = -1,$$

$$P_{\xi_\psi} A_{\xi_\psi} + A_{\xi_\psi}^T P_{\xi_\psi} = -2I_{2 \times 2}.$$

On the other hand, it is not trivial to check the stability of the $\tilde{\eta}_\psi$ boundary layer system. In order for that, the system (38) without $-\tau_\psi B_{\psi_1} \dot{\eta}_{\psi_1}^*$ is rearranged as

$$\tau_\psi \dot{\tilde{\eta}}_\psi = A_{\tilde{\eta}_\psi} \tilde{\eta}_\psi + B_{\psi_2} \Phi_\psi \quad (39)$$

where $\Phi_\psi = -a_{\psi_0} \bar{I}_z^{-1} \tilde{\eta}_{\psi_1}$. To show the stability of the above system (39), we employ circle criterion (Khalil, 2002). The graphical interpretation of the circle criterion requires a disk $\mathcal{D}(\lambda_1, \lambda_2)$ whose center is on the real axis in the complex plane. The diameter of the disk \mathcal{D} is the line segment connecting $-\bar{I}_z/I_{z_{\max}}$ and $-\bar{I}_z/I_{z_{\min}}$ ($= -1$).

Let us define $G(s)$ which is the transfer function of the system in (39) as follows

$$G(s) = \frac{a_{\psi_0}}{s(s + a_{\psi_1})}. \quad (40)$$

The coefficients a_{ψ_0} and a_{ψ_1} are determined to confine the real part of the Nyquist plot of $G(s)$ is larger than $-a_{\psi_0}/a_{\psi_1}^2$, i.e., $\Re\{G(s)\} > -a_{\psi_0}/a_{\psi_1}^2$. By setting a_{ψ_0} and a_{ψ_1} to satisfy $-1 < -a_{\psi_0}/a_{\psi_1}^2$, the Nyquist plot of $G(s)$ does not encircle, reside or is not connected with the disk \mathcal{D} . Thus, the system in (39) is exponentially stable with the circle criterion, and there exists a Lyapunov function $W_{\tilde{\eta}}$ such that

$$W_{\tilde{\eta}} = \tilde{\eta}_\psi^T P_{\tilde{\eta}_\psi} \tilde{\eta}_\psi, \quad \tau_\psi \dot{W}_{\tilde{\eta}} \leq -\lambda_\psi \|\tilde{\eta}_\psi\|^2 \quad (41)$$

where $P_{\tilde{\eta}} (\in \mathbb{R}^{2 \times 2})$ is a positive definite matrix and $\lambda_\psi > 0$. The terms $\tilde{\eta}_v^*$ and $\tilde{\eta}_{\psi_1}^*$ in (36) and (38) are bounded as follows:

$$\begin{aligned}\tilde{\eta}_v^* &= \frac{d}{dt} \left\{ m \bar{m}^{-1} F_{x_n} - F_{x_n} - m r v_y - \Delta_x \right\} \\ &\leq f_1(\cdot) e_v + f_2(\cdot) \tilde{\eta}_v + f_3(\cdot) \|e_\psi\| + f_4(\cdot) \|\tilde{\eta}_\psi\| + f_5(\cdot), \\ \tilde{\eta}_{\psi_1}^* &= \frac{d}{dt} \left\{ \bar{I}_z^{-1} I_z M_{z_n} - M_{z_n} - \Delta_z \right\} \\ &\leq f_6(\cdot) \|e_\psi\| + f_7(\cdot) \|\tilde{\eta}_\psi\| + f_8(\cdot) \end{aligned} \quad (42)$$

where $f_i(\cdot)$ is a function of $m, \bar{m}, I_z, \dot{I}_z, v_d, \dot{v}_d, \psi_d, \dot{\psi}_d, \psi_d, \dot{\psi}_d, \Delta_x, \dot{\Delta}_x, \Delta_y, \dot{\Delta}_y, \Delta_z, \dot{\Delta}_z$ and all arguments are bounded with Assumptions 1–3. In addition, to analyze the stability of the overall closed system, the error dynamics $\dot{e}_v, \dot{e}_{\psi_2}$ are rearranged as

$$\begin{aligned}\dot{e}_v &= \dot{v}_d - \dot{v}_x \\ &= \dot{v}_d - \frac{1}{m} \tilde{\eta}_v - \frac{1}{m} F_{x_n} \\ &= (1 - \alpha_v) \dot{v}_d - k_v e_v - \frac{1}{m} \tilde{\eta}_v \end{aligned} \quad (43)$$

and

$$\begin{aligned}\dot{e}_{\psi_2} &= \dot{r} - \dot{r} \\ &= \ddot{\psi}_d + k_{\psi_1} \dot{e}_{\psi_1} - \frac{1}{I_z} \tilde{\eta}_{\psi_1} - \frac{1}{I_z} M_{z_n} \\ &= (1 - \alpha_{\psi}) \ddot{\psi}_d - k_{\psi_2} e_{\psi_2} - \frac{1}{I_z} \tilde{\eta}_{\psi_1}\end{aligned}\quad (44)$$

where the employed $\dot{v}_t, \dot{r}, F_x, M_z, F_{x_n}$ and M_{z_n} are presented in (1), (31), (32), (5) and (11), respectively.

Now, we are ready to state the main results of this paper.

Theorem 1. Under Assumptions 1–3, for any given $\epsilon > 0$, there exist $k_v, \tau_v, a_v, k'_{\psi_1}, k'_{\psi_2}, \tau_{\psi}, a_{\psi_0}, a_{\psi_1}$ such that the DOB-based path controller [(5), (11), (18) and (21)] (with zero initial conditions) guarantees that

$$|v_d(t) - v_x(t)| \leq \epsilon, \quad |\psi_d(t) - \psi(t)| \leq \epsilon \quad \forall t \geq t_0 \quad (45)$$

where $v_x(t), \psi(t)$ are solutions of (1).

Proof. To evaluate the closed-loop performance with the proposed controller, consider a Lyapunov function candidate defined as

$$V = V_n + \frac{1}{2} \gamma_{\tilde{v}} \tilde{e}_v^2 + \frac{1}{2} \gamma_{\tilde{\eta}_v} \tilde{\eta}_v^2 + \frac{1}{2} \tilde{\eta}_{\psi}^T P_{\tilde{\eta}_{\psi}} \tilde{\eta}_{\psi} + \frac{1}{2} \tilde{\eta}_{\psi}^T P_{\tilde{\eta}_{\psi}} \tilde{\eta}_{\psi} \quad (46)$$

where V_n is defined in (14). Then, the directional time derivative of (46) along Eqs. (9), (43)–(44), (35)–(38) is represented as

$$\begin{aligned}\dot{V} &\leq -k_v e_v^2 + d_v |e_v| + \frac{1}{m} e_v \tilde{\eta}_v - k_{\psi} \|e_{\psi}\|^2 + d_{\psi} \|e_{\psi}\| + \frac{1}{I_z} e_{\psi_2} \tilde{\eta}_{\psi_1} \\ &\quad - \frac{1}{\tau_v} \tilde{e}_v^2 + |\gamma_{\tilde{v}} \tilde{e}_v (m^{-1} \tilde{\eta}_v + \alpha_v \dot{v}_d + k_v e_v)| - \frac{1}{\tau_v} \tilde{\eta}_v^2 + |\gamma_{\tilde{\eta}_v} \tilde{\eta}_v \tilde{\eta}_{\psi}^*| \\ &\quad - \frac{1}{\tau_{\psi}} \|\tilde{\eta}_{\psi}\|^2 \\ &\quad + |\tilde{\eta}_{\psi}^T P_{\tilde{\eta}_{\psi}} B_{\psi_2} (I_z^{-1} \tilde{\eta}_{\psi_1} + \alpha_{\psi} \ddot{\psi}_d - k_{\psi_1}^2 e_{\psi_1} + (k_{\psi_1} + k_{\psi_2}) e_{\psi_2})| \\ &\quad - \frac{\lambda_{\psi}}{\tau_{\psi}} \|\tilde{\eta}_{\psi}\|^2 + |\tilde{\eta}_{\psi}^T P_{\tilde{\eta}_{\psi}} B_{\psi_1} \dot{\eta}_{\psi}^*| \quad (47)\end{aligned}$$

where F_{x_n}, M_{z_n} in (5) and (11) are utilized. In (47), two cross terms $m^{-1} e_v \tilde{\eta}_v, I_z^{-1} e_{\psi_2} \tilde{\eta}_{\psi_1}$ are bounded as follows

$$m^{-1} e_v \tilde{\eta}_v \leq \frac{\alpha_1}{2\epsilon_1} e_v^2 + \frac{\epsilon_1}{2} \tilde{\eta}_v^2, \quad (48)$$

$$I_z^{-1} e_{\psi_2} \tilde{\eta}_{\psi_1} \leq \frac{\beta_1}{2\epsilon_4} \|\tilde{\eta}_{\psi}\|^2 + \frac{\epsilon_4}{2} \|e_{\psi}\|^2 \quad (49)$$

where $\alpha_1 := \max_t |m^{-1}(t)|$, $\beta_1 := \max_t |I_z^{-1}(t)|$ and $\epsilon_1, \epsilon_4 > 0$. For the subsequent analysis, two terms related with \tilde{e}_v and $\tilde{\eta}_v$ in (47) are rearranged as follows:

$$\begin{aligned}&\bullet |\gamma_{\tilde{v}} \tilde{e}_v (m^{-1} \tilde{\eta}_v + \alpha_v \dot{v}_d + k_v e_v)| \\ &\leq \frac{\alpha_2}{2} (\tilde{e}_v^2 + \tilde{\eta}_v^2) + \alpha_3 |\tilde{e}_v| + \left(\frac{\alpha_4}{2\epsilon_2} \tilde{e}_v^2 + \frac{\epsilon_2}{2} e_v^2 \right) \\ &= \frac{\epsilon_2}{2} e_v^2 + \left(\frac{\alpha_2}{2} + \frac{\alpha_4}{2\epsilon_2} \right) \tilde{e}_v^2 + \frac{\alpha_2}{2} \tilde{\eta}_v^2 + \alpha_3 |\tilde{e}_v| \quad (50)\end{aligned}$$

$$\begin{aligned}&\bullet |\tilde{\eta}_{\psi}^T P_{\tilde{\eta}_{\psi}} B_{\psi_2} (I_z^{-1} \tilde{\eta}_{\psi_1} + \alpha_{\psi} \ddot{\psi}_d - k_{\psi_1}^2 e_{\psi_1} + (k_{\psi_1} + k_{\psi_2}) e_{\psi_2})| \\ &\leq \frac{\beta_2}{2} (\|\tilde{\eta}_{\psi}\|^2 + \|\tilde{\eta}_{\psi}\|^2) + \beta_3 \|\tilde{\eta}_{\psi}\| + \left(\frac{\beta_4}{2\epsilon_5} \|\tilde{\eta}_{\psi}\|^2 + \frac{\epsilon_5}{2} \|e_{\psi}\|^2 \right) \\ &= \frac{\epsilon_5}{2} \|e_{\psi}\|^2 + \left(\frac{\beta_2}{2} + \frac{\beta_4}{2\epsilon_5} \right) \|\tilde{\eta}_{\psi}\|^2 + \frac{\beta_2}{2} \|\tilde{\eta}_{\psi}\|^2 + \beta_3 \|\tilde{\eta}_{\psi}\| \quad (51)\end{aligned}$$

where $\alpha_2 := \max_t |\gamma_{\tilde{v}} m^{-1}|$, $\alpha_3 := \max_t |\gamma_{\tilde{v}} m^{-1} \alpha_v \dot{v}_d|$, $\alpha_4 := \max_t |\gamma_{\tilde{v}} m^{-1} k_v|$, $\beta_2 := \max_t \|\tilde{\eta}_{\psi}^T P_{\tilde{\eta}_{\psi}} B_{\psi_2} I_z^{-1}\|$, $\beta_3 := \max_t \|\tilde{\eta}_{\psi}^T P_{\tilde{\eta}_{\psi}} B_{\psi_2} \alpha_{\psi} \ddot{\psi}_d\|$, $\beta_4 := \max \|\tilde{\eta}_{\psi}^T P_{\tilde{\eta}_{\psi}} B_{\psi_2} [k_{\psi_1}^2, k_{\psi_1} + k_{\psi_2}]\|$ and $\epsilon_2, \epsilon_5 > 0$. The terms with the time derivatives of the quasi-states $\eta_{\psi}^*, \eta_{\psi_1}^*$ are rearranged as follows:

$$\begin{aligned}&\bullet |\gamma_{\tilde{\eta}_v} \tilde{\eta}_v \tilde{\eta}_{\psi}^*| \leq |\gamma_{\tilde{\eta}_v} \tilde{\eta}_v (f_1(t) e_v + f_2(t) \tilde{\eta}_v + f_3(t) \|e_{\psi}\| + f_4(t) \|\tilde{\eta}_{\psi}\| + f_5(\cdot))| \\ &\leq \left(\frac{\alpha_5}{2\epsilon_3} \|\tilde{\eta}_v\|^2 + \frac{\epsilon_3}{2} e_v^2 \right) + \alpha_6 \|\tilde{\eta}_v\|^2 + \left(\frac{\alpha_7}{2\epsilon_7} \|\tilde{\eta}_v\|^2 \right.\end{aligned}$$

$$\begin{aligned}&\quad \left. + \frac{\epsilon_7}{2} \|e_{\psi}\|^2 \right) + \frac{\alpha_8}{2} (\|\tilde{\eta}_v\|^2 + \|\tilde{\eta}_{\psi}\|^2) + \alpha_9 |\tilde{\eta}_v| \\ &\leq \frac{\epsilon_3}{2} e_v^2 + \frac{\epsilon_7}{2} \|e_{\psi}\|^2 + \left(\frac{\alpha_5}{2\epsilon_3} + \alpha_6 + \frac{\alpha_7}{2\epsilon_7} + \frac{\alpha_8}{2} \right) \tilde{\eta}_v^2 + \frac{\alpha_8}{2} \|\tilde{\eta}_{\psi}\|^2 \\ &\quad + \alpha_9 |\tilde{\eta}_v| \quad (52)\end{aligned}$$

$$\begin{aligned}&\bullet |\tilde{\eta}_{\psi}^T P_{\tilde{\eta}_{\psi}} B_{\psi_1} \dot{\eta}_{\psi}^*| \leq |\tilde{\eta}_{\psi}^T P_{\tilde{\eta}_{\psi}} B_{\psi_1} (f_6(t) \|e_{\psi}\| + f_7(t) \|\tilde{\eta}_{\psi}\| + f_8(\cdot))| \\ &\leq \left(\frac{\beta_5}{2\epsilon_6} \|\tilde{\eta}_{\psi}\|^2 + \frac{\epsilon_6}{2} \|e_{\psi}\|^2 \right) + \beta_6 \|\tilde{\eta}_{\psi}\|^2 + \beta_7 \|\tilde{\eta}_{\psi}\| \\ &\leq \frac{\epsilon_6}{2} \|e_{\psi}\|^2 + \left(\frac{\beta_5}{2\epsilon_6} + \beta_6 \right) \|\tilde{\eta}_{\psi}\|^2 + \beta_7 \|\tilde{\eta}_{\psi}\| \quad (53)\end{aligned}$$

where $\alpha_5 := \max_t |\gamma_{\tilde{\eta}_v} f_1(t)|$, $\alpha_6 := \max_t |\gamma_{\tilde{\eta}_v} f_2(t)|$, $\alpha_7 := \max_t |\gamma_{\tilde{\eta}_v} f_3(t)|$, $\alpha_8 := \max_t \|\gamma_{\tilde{\eta}_v} f_4(t)\|$, $\alpha_9 := \max_t |\gamma_{\tilde{\eta}_v} f_5(t)|$, $\beta_5 := \max_t \|\tilde{\eta}_{\psi}^T P_{\tilde{\eta}_{\psi}} B_{\psi_1} f_6(t)\|$, $\beta_6 := \max_t \|\tilde{\eta}_{\psi}^T P_{\tilde{\eta}_{\psi}} B_{\psi_1} f_7(t)\|$, $\beta_7 := \max_t \|\tilde{\eta}_{\psi}^T P_{\tilde{\eta}_{\psi}} B_{\psi_1} f_8(t)\|$ and $\epsilon_3, \epsilon_6, \epsilon_7 > 0$. Then, with the Eqs. (48)–(53), the directional time derivative (47) is bounded as follows:

$$\begin{aligned}\dot{V} &\leq -\lambda_1 e_v^2 - \lambda_2 \tilde{e}_v^2 - \lambda_3 \tilde{\eta}_v^2 + d_v |e_v| + \alpha_3 |\tilde{e}_v| + \alpha_9 |\tilde{\eta}_v| - \lambda_4 \|e_{\psi}\|^2 - \lambda_5 \|\tilde{\eta}_{\psi}\|^2 \\ &\quad - \lambda_6 \|\tilde{\eta}_{\psi}\|^2 + d_{\psi} \|e_{\psi}\| + \beta_3 \|\tilde{\eta}_{\psi}\| + \beta_7 \|\tilde{\eta}_{\psi}\| \quad (54)\end{aligned}$$

where

$$\begin{aligned}\lambda_1 &= k_v - \frac{\epsilon_1 + \epsilon_2 + \epsilon_3}{2}, \\ \lambda_2 &= \frac{1}{\tau_v} - \frac{\alpha_2}{2} - \frac{\alpha_4}{2\epsilon_2}, \\ \lambda_3 &= \frac{1}{\tau_v} - \frac{\alpha_1}{2\epsilon_1} - \frac{\alpha_2}{2} - \frac{\alpha_5}{2\epsilon_3} - \alpha_6 - \frac{\alpha_7}{2\epsilon_7} - \frac{\alpha_8}{2}, \\ \lambda_4 &= k_{\psi} - \frac{\epsilon_4 + \epsilon_5 + \epsilon_6 + \epsilon_7}{2}, \\ \lambda_5 &= \frac{1}{\tau_{\psi}} - \frac{\beta_2}{2} - \frac{\beta_4}{2\epsilon_5}, \\ \lambda_6 &= \frac{\lambda_{\psi}}{\tau_{\psi}} - \frac{\beta_1}{2\epsilon_4} - \frac{\beta_2}{2} - \frac{\beta_5}{2\epsilon_6} - \beta_6 - \frac{\alpha_8}{2}.\end{aligned}\quad (55)$$

To assure that $\lambda_i > 0 (i = 1, \dots, 6)$ and $k_v, k_{\psi} > 1$, we can select $k_v, \tau_v, k_{\psi}, \tau_{\psi}$ as follows:

$$\begin{aligned}k_v &> \max \left\{ 1, \frac{\epsilon_1 + \epsilon_2 + \epsilon_3}{2} \right\}, \\ \frac{1}{\tau_v} &> \max \left\{ \frac{\alpha_2}{2} + \frac{\alpha_4}{2\epsilon_2}, \frac{\alpha_1}{2\epsilon_1} + \frac{\alpha_2}{2} + \frac{\alpha_5}{2\epsilon_3} + \alpha_6 + \frac{\alpha_7}{2\epsilon_7} + \frac{\alpha_8}{2} \right\}, \\ k_{\psi} &> \max \left\{ 1, \frac{\epsilon_4 + \epsilon_5 + \epsilon_6 + \epsilon_7}{2} \right\}, \\ \frac{1}{\tau_{\psi}} &> \max \left\{ \frac{\beta_2}{2} + \frac{\beta_4}{2\epsilon_5}, \frac{1}{\lambda_{\psi}} \left(\frac{\beta_1}{2\epsilon_4} + \frac{\beta_2}{2} + \frac{\beta_5}{2\epsilon_6} + \beta_6 + \frac{\alpha_8}{2} \right) \right\}.\end{aligned}\quad (56)$$

For the subsequent analysis, define new variable $Y \triangleq [e_v, \tilde{e}_v, \tilde{\eta}_v, e_{\psi}, \tilde{\eta}_{\psi}]^T$ and

$$\lambda \triangleq \min_{i=1, \dots, 6} \lambda_i, \quad \kappa \triangleq d_v + \alpha_3 + \alpha_9 + d_{\psi} + \beta_3 + \beta_7. \quad (57)$$

Thus, the above bounded Eq. (54) is bounded as $\dot{V} \leq -\lambda \|Y\|^2 + \kappa \|Y\|$, which means that, if $\|Y\| > \kappa/\lambda$, $\dot{V} < 0$. With this property, the equation related to the Lyapunov function value is obtained as follows:

$$\begin{aligned}\max_{\|Y\|=\kappa/\lambda} V(Y) &\leq \frac{1}{2} \max_{\|Y\|=\kappa/\lambda} \left(e_v^2 + \gamma_{\tilde{v}} \tilde{e}_v^2 + \gamma_{\tilde{\eta}_v} \tilde{\eta}_v^2 + \|e_{\psi}\|^2 \right. \\ &\quad \left. + \tilde{\eta}_{\psi}^T P_{\tilde{\eta}_{\psi}} \tilde{\eta}_{\psi} + \tilde{\eta}_{\psi}^T P_{\tilde{\eta}_{\psi}} \tilde{\eta}_{\psi} \right) \\ &\triangleq \mu,\end{aligned}\quad (58)$$

where μ is a positive constant. We define the set $\Omega_{\mu} \triangleq \{Y : V(Y) \leq \mu\}$. Then, it is evident for any solution initiated within Ω_{μ} to remain in Ω_{μ} . Since all the initial velocity and heading angle commands start from the initial velocity and heading angle, the solution of the closed-loop systems begins at the origin and remains within Ω_{μ} . The result implies that, for all $Y \in \Omega_{\mu}$,

$$\frac{1}{2} e_v^2 \leq V(Y) \leq \mu \quad \text{and} \quad \frac{1}{2} e_{\psi_1}^2 \leq \frac{1}{2} \|e_{\psi}\|^2 \leq V(Y) \leq \mu \quad (59)$$



Fig. 5. Vertical force sensors.



Fig. 6. Proving ground: (a) proving ground A, (b) proving ground B.

and thus, $|e_v| = |v_d(t) - v(t)| \leq \sqrt{2\mu}$ and $|e_{\psi}| = |\psi_d(t) - \psi(t)| \leq \sqrt{2\mu}$. Finally, for a given ϵ , it is always possible to choose $k_v, \tau_v, k_\psi, \tau_\psi$ by (56) for assuring $\mu \leq \epsilon^2/2$ because $k_v, k_\psi \rightarrow \infty$ and $\tau_v, \tau_\psi \rightarrow 0$ imply $\kappa/\lambda \rightarrow 0$ and $\mu \rightarrow 0$ due to (57) and (58). ■

Remark 2. As addressed in Remark 1, the nominal controller assures that the errors e_v and e_ψ of the closed-loop system with the nominal system go to the value less than or equal to ϵ . Through the Theorem 1, we confirm that, for a given ϵ , the errors e_v and e_ψ of the closed-loop system with the uncertain nonlinear system converge to the value less than or equal to ϵ by adding the DOB to the nominal controller. The result implies that the proposed path controller recovers the nominal performance of the uncertain nonlinear AGV by incorporating the nominal controller with the disturbance observer.

Remark 3. To determine the control input F_x (18) and M_z (21), the parameters $k_v, \alpha_v, \tau_v, a_v, k_\psi, \alpha_\psi, \tau_\psi, a_{\psi_0}, a_{\psi_1}$ should be designed appropriately. In order for that, k_v and k_ψ are designed first as the value larger than 1 with sufficiently small $\epsilon_i (i = 1, \dots, 7)$, i.e., $\sum_{i=1}^3 \epsilon_i/2 \leq 1, \sum_{j=4}^7 \epsilon_j/2 \leq 1$ (e.g., $\epsilon_i = 2/3, \epsilon_j = 1/2$). The gains α_v, α_ψ are determined as numbers close to 1 to cancel the desired command $\dot{v}_d, \dot{\psi}_d$. While a_v is a positive constant, a_{ψ_0}, a_{ψ_1} are set to positive constant values for satisfying the constraint $a_{\psi_1}^2 > a_{\psi_0}$. Finally, the values $\alpha_i (i = 1, \dots, 8), \beta_j (j = 1, \dots, 7)$ are need to choose τ_v, τ_ψ . They can be computed with the information of $\gamma_{\tilde{v}}, \gamma_{\tilde{\psi}}, P_{\tilde{v}}, P_{\tilde{\psi}}$ and bounds of $f_i(\cdot) (i = 1, \dots, 8)$ which can be estimated by the control gains and dynamic test of the AGV. However, it would be a nontrivial and time-consuming task to compute the values τ_v, τ_ψ . Instead, we recommend that a practical engineer would design those values using simulations or experiments because sufficiently small τ_v, τ_ψ always satisfies (56) when the gains $k_v, \alpha_v, k_\psi, \alpha_\psi$ are determined.

3.3. Tire force distribution

The total force F_x and moment M_z are composed of $F_{x_i} (i = 1, \dots, 6)$ and represented as

$$F_x = F_{x_1} + F_{x_2} + F_{x_3} + F_{x_4} + F_{x_5} + F_{x_6}, \quad (60)$$

$$M_z = \frac{t_w}{2} (F_{x_1} - F_{x_2} + F_{x_3} - F_{x_4} + F_{x_5} - F_{x_6}). \quad (61)$$

They mean that the final control inputs enabling the AGV to move are the tire force $F_{x_i} (i = 1, \dots, 6)$. Thus, to follow the velocity and heading angle commands, the control inputs (18), (21) should be distributed to the tire forces $F_{x_i} (i = 1, \dots, 6)$.

To determine the tire force F_{x_i} , this study utilizes a solution of an optimal tire force distribution problem defined as

$$\min_{F_{x_i}} J \quad (62)$$

where

$$J = \frac{1}{2} F^T W_z F, \quad (63)$$

$$F = [F_{x_1} \quad F_{x_2} \quad F_{x_3} \quad F_{x_4} \quad F_{x_5} \quad F_{x_6}], \quad (64)$$

$$W_z = \text{diag} \{1/F_{z_1} \quad \dots \quad 1/F_{z_6}\} \quad (65)$$

and $F_{z_i} (i = 1, \dots, 6)$ denotes vertical force acting on each tire. The total force F_x and moment M_z shown in (60) and (61) are utilized as an equality constraint as follows:

$$\begin{bmatrix} F_x \\ M_z \end{bmatrix} = BF \quad (66)$$

where

$$B = \begin{bmatrix} 1 & 1 & 1 & 1 & 1 & 1 \\ \frac{t_w}{2} & -\frac{t_w}{2} & \frac{t_w}{2} & -\frac{t_w}{2} & \frac{t_w}{2} & -\frac{t_w}{2} \end{bmatrix}.$$

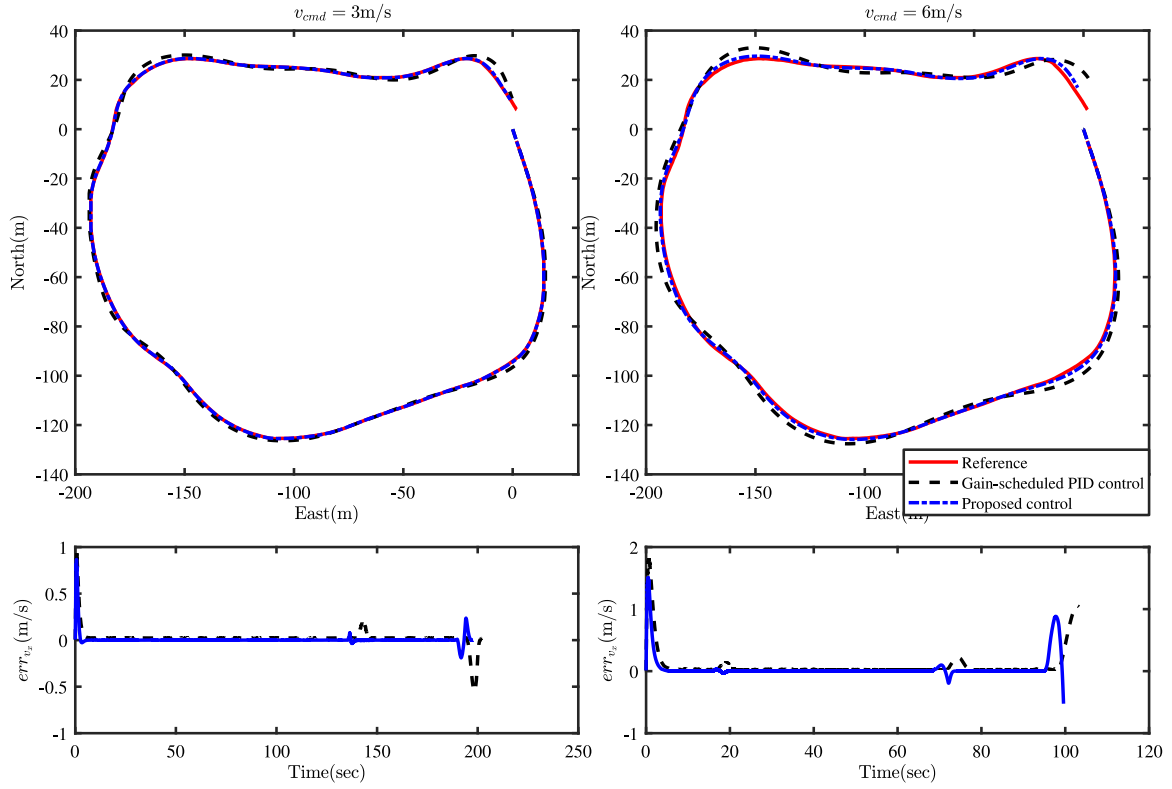


Fig. 7. Trajectory and velocity error histories: Numerical simulation.

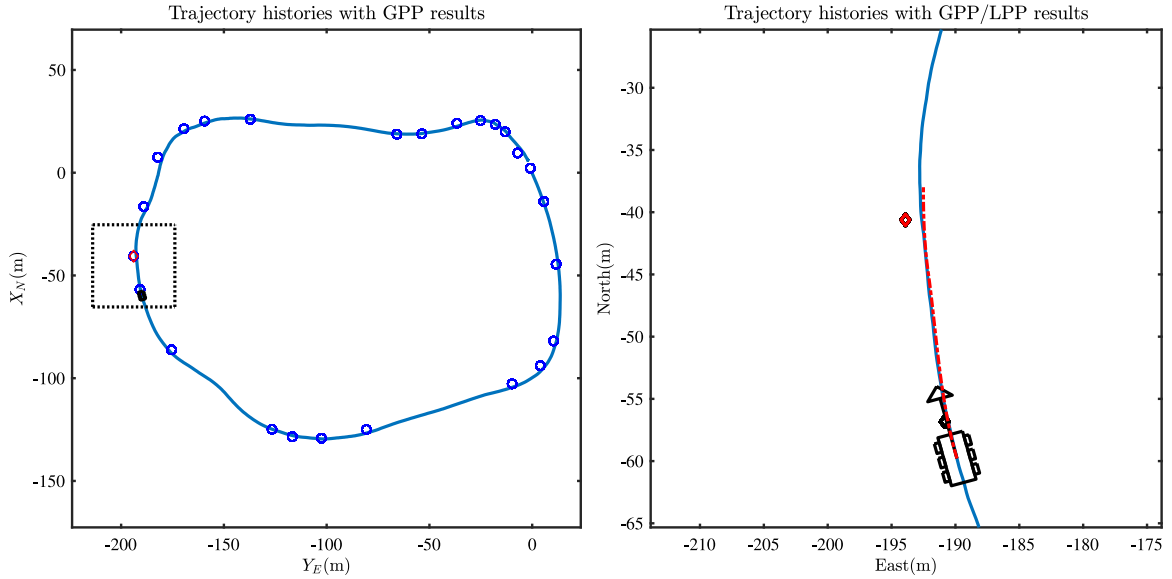


Fig. 8. Trajectory histories: Proving ground A.

In addition, to limit the maximum or minimum value of the tire force, inequality constraints are derived as

$$F_{x_i} \leq F_{\max}, \quad F_{x_i} \geq F_{\min}$$

where F_{\max} , F_{\min} denote the maximum and minimum values of the tire force, respectively. The cost function in (63) denotes that the larger F_{z_i} is measured, the larger F_{x_i} is provided, because, according to the driving environment or attitude/velocity of the AGV, some tires possess large vertical forces, others have small vertical forces, or there can exist the tires which are not on the ground. On the other hand, it is not trivial to obtain a solution of the above optimal problem because it has several

equality and inequality constraints. To handle the problem, this study utilizes the CVXGEN tool developed in [Mattingale and Boyd \(2018\)](#). The CVXGEN tool is a well known method to solve a general optimization problem.

The above optimization problem requires the vertical force F_{z_i} of each tire. In this study, a vertical force transducer, commercially obtainable in [TruckSim \(0000b\)](#), is installed at the rim of each tire and presented in [Fig. 5](#). The vertical forces are measured at 100 Hz and utilized in the optimization problem.

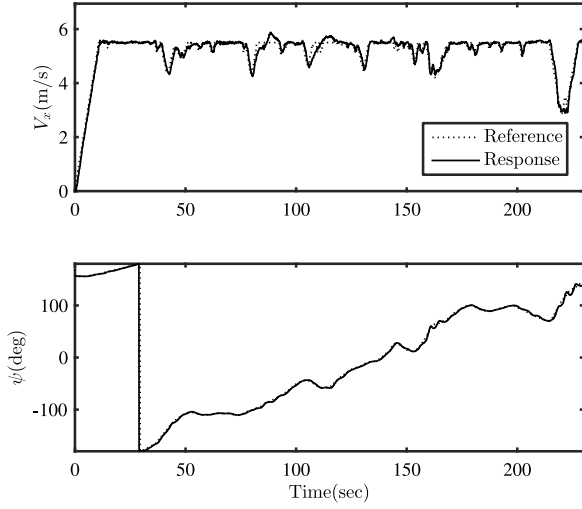


Fig. 9. Velocity & heading angle histories: Proving ground A.

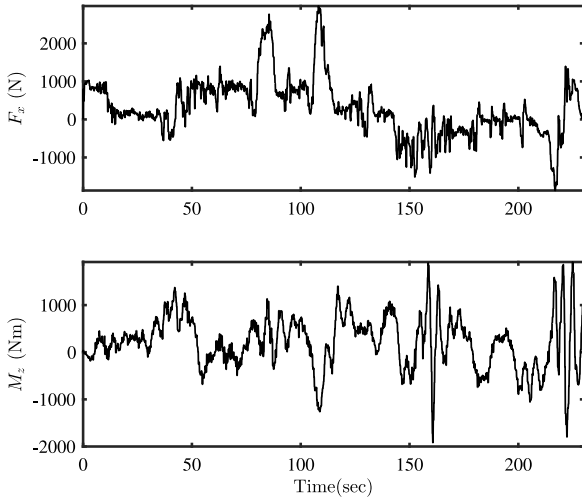


Fig. 10. Control input histories: Proving ground A.

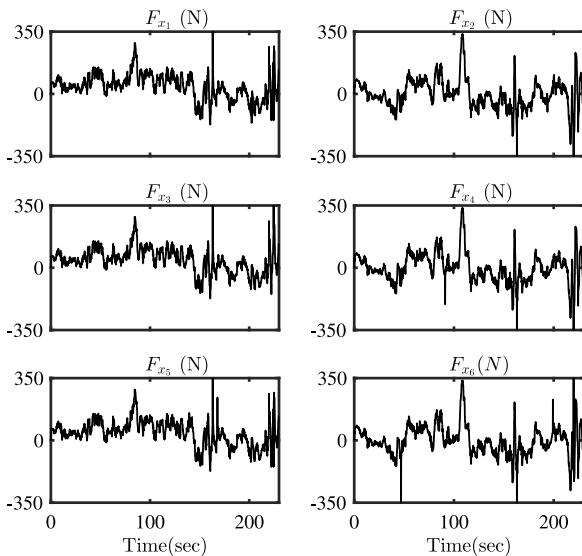


Fig. 11. Traction force histories: Proving ground A.

4. Validation

In this section, experimental setup and results are described to validate the performance of the proposed method.

4.1. Validation setup

The skid-type AGV shown in Fig. 5 is utilized in the validation. The weight of the AGV is over 5000 kg, and the maximum velocity is about 40–50 KPH. The AGV is powered by a serial-type hybrid engine which is composed of battery and gasoline engine, and the battery is charged by the gasoline engine.

To validate the performance of the proposed method, the numerical simulation is conducted first using the TruckSim software (TruckSim, 0000a) which is widely utilized in the automobile company. The reference path for the simulation is set to the real trajectory obtained from the operation of the AGV in proving ground A developed by the authors' laboratory as shown in Fig. 6. The gains in the numerical simulations are designed as follows:

$$k_v = 10, a_v = 1, \tau_v = 0.5,$$

$$k_{\psi_1} = 20, k_{\psi_2} = 15, a_{\psi_0} = 1, a_{\psi_1} = 2, \tau_{\psi} = 0.5.$$

where the above gains were determined with several numerical simulations for following the given trajectory of the proving ground A.

On the other hand, the field tests are conducted both at the proving ground A and B. For the field tests, several sensors such as the IMU, GPS, 2/3D scanner, CCD cameras and magnetometers are installed at the AGV to perceive or measure the AGV's own states and unknown environments. As expected, the field tests require the robust and steady inertial state information of the AGV, but it is not trivial to assure the consistency of the navigation information of the AGV in the outdoor environment. In order to handle that, the GPS/INS integrated system has been widely used in outdoor environment (Grewall, Weill, & Andrews, 2007). However, its robustness and accuracy are not guaranteed because the GPS data are vulnerable to the external disturbances. To compensate this problem, this study utilizes the multi-sensor fusion algorithm which follows the different operating principle (Choi, Park, Kim, Choe, & Song, 0000). The gains in the proposed controller are designed as follows:

$$k_v = 6, a_v = 1, \tau_v = 0.1,$$

$$k_{\psi_1} = 6, k_{\psi_2} = 6, a_{\psi_0} = 1, a_{\psi_1} = 2, \tau_{\psi} = 0.1.$$

They were determined with some field tests for following several constant waypoints at open space.

4.2. Validation results

The proposed method requires appropriate velocity and heading angle commands. As addressed in the above, the velocity command is simply set by the operator and the heading angle command is determined using the current position of the AGV and next waypoint.

To perform the numerical simulations, one point of the given trajectory which is at specific meters from the current AGV position is chosen as the next waypoint. On the other hand, in the field test, the heading angle command is determined using the local path planning results obtained by the method in Ref. Shin et al. (2020). The path is composed of 40 reference points which are generated by employing the AGV dynamic model with the constant velocity command and one point among them is chosen by checking the distance from the current AGV position. Then, the desired heading angle command is determined as in the following manner:

$$\psi_d = \text{atan2}(w_E^k - y_E, w_N^k - x_N) \quad (67)$$

where $\text{atan2}(\cdot, \cdot)$ is an inverse function of the tangent function defined between $-\pi$ and π . Even though w_N^k, w_E^k denote north and east position

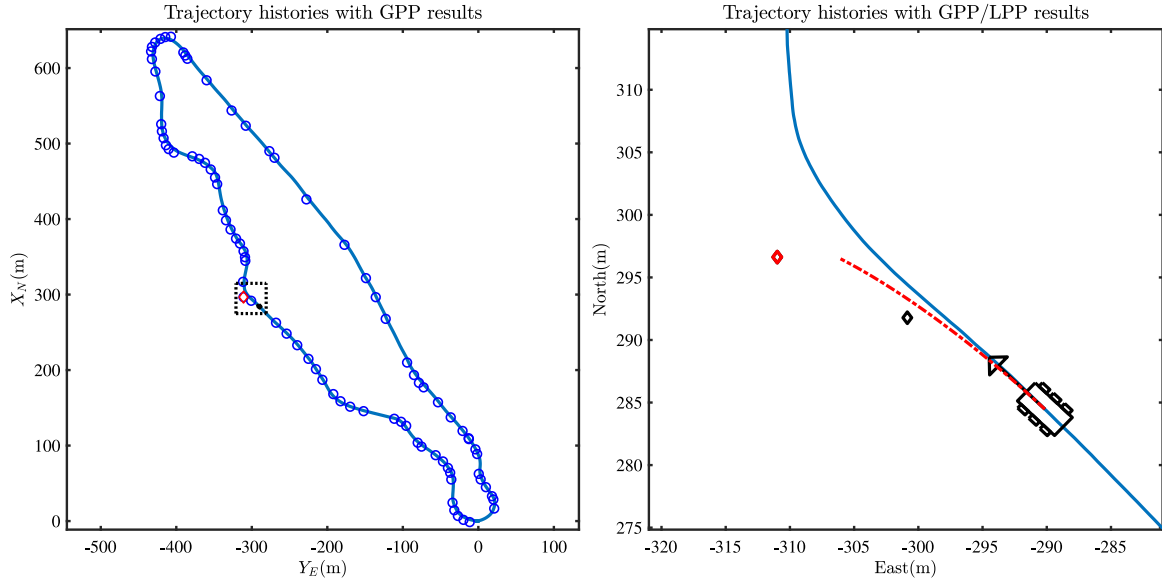


Fig. 12. Trajectory histories: Proving ground B.

of one point among the given trajectory in the numerical simulation, they describe north and east position of k th point among the local path results in the field test.

On the other hand, as addressed in Shin et al. (2020), the constant velocity command is adjusted with the LPP results and environment perception results. The adjustment in this study is called traversability analysis and its detailed explanation is presented in Hong et al. (2017). Then, the given adjusted velocity and heading angle commands are filtered and followed by the proposed controller. However, the numerical simulation studies utilize the constant velocity command only, because it is not trivial to develop the simulator for integrating the overall autonomous navigation technologies such the perception, planning and control.

4.2.1. Numerical simulation

To validate the performance of the proposed method, numerical simulations were conducted first. The trajectory obtained by the manned driving of the AGV was set to the reference and utilized for the generation of the heading angle command, and the velocity commands were set to 3 m/s and 6 m/s. Additionally, the results with the proposed controller were compared with the gain scheduled PID control method developed on (Rotem, 0000).

As shown in Fig. 7, the performance of the proposed method is better than that of the gain-scheduled PID control method because it is not trivial to find the weight or rule for adjusting the control gains at all situation. Especially, as the velocity command is increased, the performance difference between them becomes larger. This is because, according to the increment of the velocity, the path controller should handle larger dynamic characteristics of the AGV. Based on the numerical simulation results, the field tests were performed with the proposed controller only.

4.2.2. Field tests

The first test was performed at the proving ground A and the velocity command by the operator was set to 5.5 m/s. Figs. 8–11 show the results of the first experiment. The position trajectory of the AGV during the autonomous navigation is presented in Fig. 8. In Fig. 8, the GPP and LPP results (Shin et al., 2020) are plotted with the real trajectory of the AGV. The LPP results are presented as red-line in Fig. 8, and the blue circles and red diamond denote the overall GPP results and the current target point of the AGV, respectively. The autonomous navigation was initiated from (0,0) point and the AGV

followed the given velocity and heading angles commands. As shown in Fig. 9, the heading angle commands for the autonomous navigation were determined well and its following performance is satisfactory. In addition, even though the velocity command by the operator is constant, we confirmed that the velocity command was well adjusted by the traversability analysis algorithm and the performance of the velocity control is satisfactory. The control input history corresponding to the autonomous navigation is presented in Figs. 10, and 11 shows the optimally distributed tire forces.

To validate the consistent performance of the proposed method, the field test was conducted at the proving ground B, and the velocity command by the operator was set to 6.0 m/s. The results in the proving ground B are presented in Figs. 12–15. During the autonomous navigation, the logged position history of the AGV and GPP/LPP results are presented simultaneously in Fig. 12. The trajectory history is initiated at (0,0) point and generated by following the given velocity and heading angle commands. The reference command and state histories are shown in Fig. 13. With these results, we conclude that the heading angle commands for maintaining the autonomous navigation of the AGV were determined well and followed satisfactorily, and the performance of the velocity control is satisfactory. Fig. 14 presents the control input histories during the autonomous navigation, and the final optimal traction force time histories are shown in Fig. 15.

5. Conclusion

In this study, we developed the robust velocity and heading angle controller for the AGV in the rough terrain. Because there are lots of uncertainties in the rough terrain, the robustness of the path control system is absolutely required and the DOB-based control method was proposed to improve the robustness against those uncertainties. The developed controller was designed with the two steps: the first step is to design the controller for the nominal system and the second step is to add the DOB to the nominal controller. By adding the DOB concept to the nominal controller, the nominal performance of the AGV was recovered, and the satisfactory transient response was obtained. In addition, the optimal tire force distribution problem was defined with several equality and inequality constraints, and its solution was obtained by the CVXGEN tool. Finally, the proposed path controller was validated through the numerical simulations and field tests in the rough terrain.

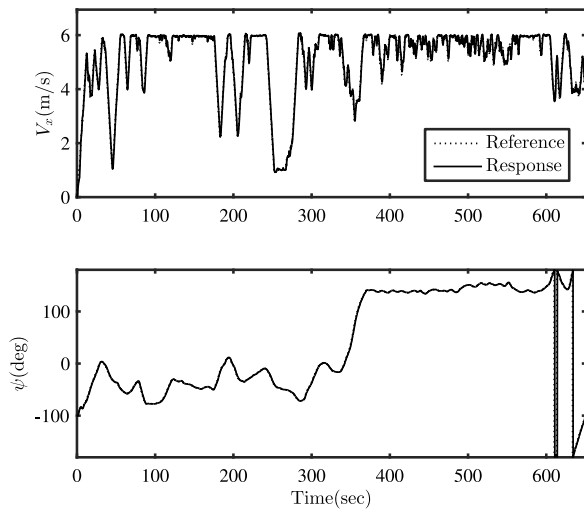


Fig. 13. Velocity & heading angle histories: Proving ground B.

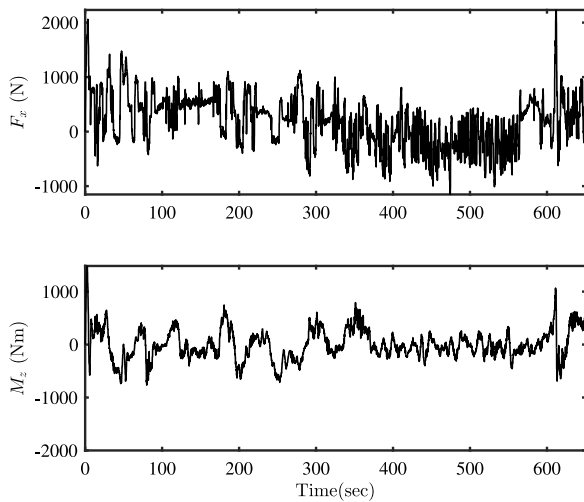


Fig. 14. Control input histories: Proving ground B.

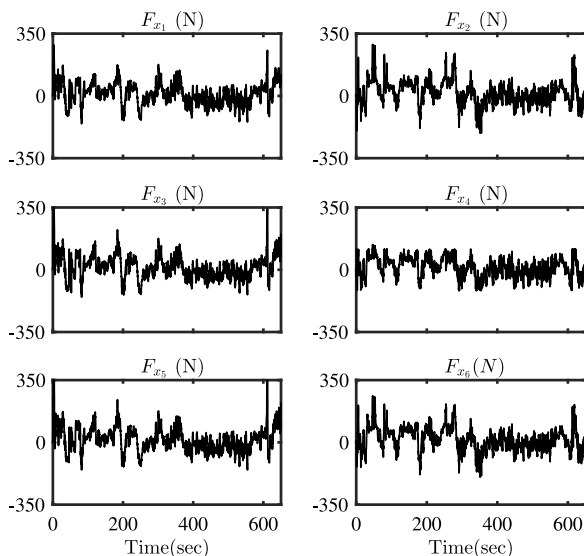


Fig. 15. Traction force histories: Proving ground B.

Declaration of competing interest

The authors declare that they have no known competing financial interests or personal relationships that could have appeared to influence the work reported in this paper.

Appendix A. Supplementary data

Supplementary material related to this article can be found online at <https://doi.org/10.1016/j.conengprac.2020.104384>.

References

- Back, J., & Shim, H. (2008). Adding robustness to nominal output-feedback controllers for uncertain nonlinear systems: A nonlinear version of disturbance observer. *Automatica*, 44(10), 2528–2537.
- Back, J., & Shim, H. (2009). An inner-loop controller guaranteeing robust transient performance for uncertain mimo nonlinear systems. *IEEE Transactions on Automatic Control*, 54, 1601–1607.
- Chen, X., Komoda, S., & Fukuda, T. (2000). Design of a nonlinear disturbance observer. *IEEE Transactions on Industrial Electronics*, 47, 429–437.
- Choi, J., Park, Y., Kim, J., Choe, T., & Song, J. Federated-filter-based unmanned ground vehicle localization using 3d range estimation with digital elevation model in outdoor environment. *Journal of Field Robotics*, 29, 298–314.
- Gonzalez, D., Perez, J., Milanes, V., & Nashashibi, F. (2016). A review of motion planning techniques for automated vehicles. *IEEE Transactions on Intelligent Transportation Systems*, 17, 1135–1145.
- Grewall, M. S., Weill, L. R., & Andrews, A. P. (2007). *Global positioning systems, inertial navigation and integration* (2nd ed.). New Jersey: Wiley-Interscience.
- Hong, H., et al. (2016). Multibody dynamics and control model of 6×6 unmanned ground vehicle for real-time traversability analysis. In *Proceedings of the 8th Asian conference on multibody dynamics*.
- Hong, H., et al. (2017). An optimal velocity profile design for 6×6 unmanned ground vehicle based on real-time traversability analysis. In *Proceedings of ECCOMAS thematic conference on multibody dynamics*.
- Huang, J., Wen, C., Wang, W., & Jiang, Z. (2014). Adaptive output feedback tracking control of a nonholonomic mobile robot. *Automatica*, 50, 821–831.
- Huang, X., Zhang, H., Zhang, G., & Wang, J. (2014). Robust weighted gain-scheduling control of vehicle lateral motion control with gain-scheduling energy-to-peak control of vehicle lateral dynamic stabilization. *IEEE Transactions on Control Systems Technology*, 22, 1740–1753.
- Iagnemma, K., & Dubowsky, S. (2004). Mobile robots in rough terrain. *Springer Tracts in Advanced Robots*.
- Kang, J., Kim, W., Lee, J., & Yi, K. (2010). Skid steering-based control of a robotic vehicle with six in-wheel drives. *IMEchE, Part D: Journal of Automobile Engineering*, 224, 1369–1391.
- Katrakazas, C., Quddus, M., Chen, W., & Deka, L. (2015). Real-time motion planning methods for autonomous on-road driving: State-of-the-art and future research directions. *Transportation Research Part C: Emerging Technologies*, 60, 416–442.
- Kayacan, E., Ramon, H., & Saeys, W. (2016). Robust trajectory tracking error model-based predictive control for unmanned ground vehicles. *IEEE/ASME Transactions on Mechatronics*, 21, 806–814.
- Khalil, H. K. (2002). *Nonlinear systems* (3rd ed.). Upper Saddle River (NJ): Prentice Hall.
- Kim, S., Seo, H., Shin, J., & Kim, H. J. (2018). Cooperative aerial manipulation using multirotors with multi-dof robotic arms. *IEEE/ASME Transactions on Mechatronics*, 23, 702–713.
- Mattingale, J., & Boyd, S. (2018). Cvxgen: A code generator for embedded convex optimization. *Optimization and Engineering*, 13, 702–713.
- Rotem, H. <http://www.hyundai-rotem.co.kr/en>.
- Shin, J., Huh, J., & Park, Y. (2015). Asymptotically stable path following for lateral motion of an unmanned ground vehicle. *Control Engineering Practice*, 40, 102–112.
- Shin, J., Kwak, D., & Kwak, K. (2020). Model predictive path planning for an autonomous ground vehicle in rough terrain. *Control Engineering Practice*, (submitted for publication).
- Sock, J., Kim, J., Min, J., & Kwak, K. (2016). Probabilistic traversability map generation using 3d-lidar and camera. In *Proceedings of IEEE international conference on robotics and automation*.
- Thrun, S., et al. (2006). Stanley: The robot that won the darpa grand challenge. *Journal of Field Robotics*, 29, 661–692.
- TruckSim, <http://www.carsim.com>.
- TruckSim, <http://www.actssystem.co.kr>.
- Urmson, C., et al. (2006). A robust approach to high-speed navigation for unrehearsed desert terrain. *Journal of Field Robotics*, 23, 467–507.
- Yi, J., Song, D., Zhang, J., & Goodwin, Z. (2007). Adaptive trajectory tracking control of skid-steered mobile robots. In *Proceedings of IEEE international conference on robotics and automation* (pp. 3310–3317).
- Zhang, H., Zhang, Z., & Wang, J. (2014). Robust gain-scheduling energy-to-peak control of vehicle lateral dynamic stabilization. *Vehicle System Dynamics*, 52, 309–340.